Friction
https://doi.org/10.1007/s40544-024-0911-6
ISSN 2223-7690
CN 10-1237/TH
RESEARCH ARTICLE

Topographic variation and fluid flow characteristics in rough contact interface

Jiawei JI, Wei SUN, Yu DU, Yongqing ZHU, Yuhang GUO, Xiaojun LIU, Yunlong JIAO*, Kun LIU
Institute of Tribology, School of Mechanical Engineering, Hefei University of Technology, Hefei 230009, China
Received: 12 December 2023 / Revised: 23 January 2024 / Accepted: 10 April 2024
© The author(s) 2024.

Abstract: Understanding flow characteristics of fluid near rough contact is important for the design of fluid-based lubrication and basic of tribology physics. In this study, the spreading and seepage processes of anhydrous ethanol in the interface between glass and rough PDMS are observed by a homemade optical *in-situ* tester. Digital image processing technology and numerical simulation software are adapted to identify and extract the topological properties of interface and thin fluid flow characteristics. Particular attention is paid to the dynamic evolution of the contact interface morphology under different stresses, the distribution of microchannels in the interface, the spreading characteristics of the fluid in contact interface, as well as the mechanical driving mechanism. Original surface morphology and the contact stress have a significant impact on the interface topography and the distribution of interfacial microchannels, which shows that the feature lengths of the microchannels, the spreading area and the spreading rate of the fluid are inversely proportional to the load. And the flow path of the fluid in the interface is mainly divided into three stages: along the wall of the island, generating liquid bridges, and moving from the tip side to the root side in the wedge-shaped channel. The main mechanical mechanism of liquid flow in the interface is the equilibrium between the capillary force that drives the liquid spreading and viscous resistance of solid wall to liquid. In addition, the phenomenon of "trapped air" occurs during the flow process due to the irregular characteristics of the microchannel. This study lays a certain theoretical foundation for the research of microscopic flow behavior of the liquid in the rough contact interface, the friction and lubrication of the mechanical system, and the sealing mechanism.

Keywords: rough contact interface; fluid flow; topography evolution; microchannel; *in-situ* observation

1 Introduction

The thin fluid flow in rough contact interface is a complex topic of microscale physics, which exists in a wide range of natural and industrial applications, including mechanical system manufacturing and equipment sealing [1, 2], microfluidic chips in biomedicine and chemical synthesis [3], as well as the extraction of oil and gas resources and the remediation of groundwater contamination in geoscience [4, 5]. When a rough surface is pressed against the other, the surface micro-convex bodies (i.e., asperities) preferentially contact and load thus resulting in smaller real contact area than the nominal area as well as free volume near the contact, in which some of free volume connected can form microchannels. In the presence of liquids or even humidity, the thin fluid would flow in the microchannels due to the capillary driving force with effects on the contact behaviors including adhesion and friction [6]. Therefore, understanding the fluid flow characteristics in the contact interface and the underlying mechanisms is important for the development of related engineering and equipment.

* Corresponding author: Yunlong JIAO, E-mail: jiaoyunlong@hfut.edu.cn

The fluid flow in the contact interface is essentially a coupling between the liquid and the solid, which is mainly affected by various factors, such as surface roughness, interface topography, contact pressure and other external environmental factors. For example, Persson et al. [7] investigated the elastic interaction between the solid surfaces based on the contact mechanics model and the fluid conductivity tensor, which first resolved the effect of disorder on the fluid flow. Dapp et al. [8] studied the liquid flow between randomly rough elastic solids by numerical simulation on the basis of percolation theory. It was found that the liquid flow at the contact interface can be reliably estimated by slightly modifying the Bruggeman's effective medium solution and the Persson contact mechanics theory. Shvarts et al. theoretically investigated pressure driven flow in a wavy channel and derived fluid pressure distributions for the case of strong coupling between fluid flow and solid deformation [9], and developed a finite-element framework for the treatment of thin fluid flow in narrow interfaces [10]. Huang et al. investigated the elastic contact of the anisotropic bisinusoidal surfaces by capturing the critical fluid pressure of fluid flow in the sealing contact surfaces [11, 12]. It could be seen that all of the above studies used numerical simulation to investigate fluid flow characteristics in rough contact interface.

Recently, capillary microfluidics has received wide attention and capillary microfluidic chips offer great potential in biomedicine, chemical synthesis, and other fields due to their advantages of low cost and ease of batch fabrication. Fluid flow near the contact is driven by the surface tension effect between the fluid and microchannels, which can be affected by surface microstructure and physicochemical properties. Therefore, extensive studies were focused on the effects of microchannel geometries on the flow characteristics of fluid [13]. The theory of capillary flow was first quantitatively investigated by Lucas and Washburn as early as the beginning of the 20th century and the Lucas–Washburn (L–W) model was established to describe the relationship between flow distance and time [14, 15]. Zhu et al. [16] compared the behaviors of fluid flowing in the glass, polycarbonate (PC), and polydimethylsiloxane (PDMS) microchannels and found that the channel shape and surface wetting properties have an important influence on the flow characteristics. A semi-analytical method proposed by Zhong et al. [17] can derive the capillary surface tension and the parallel flow resistance. Pasias et al. [18] investigated the differences in the flow of both non-Newtonian fluid and Newtonian fluid references in rectangular microchannel, which highlights the importance of capillary effects in the fluid flow. Based on capillary theory, Papadimitriou [19] used capillary valves to create immuno-detection devices by demonstrating various shapes of microchannels. It was suggested that the microchannel geometry and surface properties have a great effect on the flow characteristics of interfacial liquid. More recently, Wang et al. [20] conducted detailed experimental and numerical analysis on the imbibition behavior in a corrugated capillary tube, and constructed the quantitative variation laws of Tolman length with the increasing curvature radius of liquid–gas interface.

Despite plenty of researches have been conducted on the fluid spreading behavior at rough contact interface, many questions still remain: (1) At present, most scholars studied the liquid flow behavior through numerical simulation, the construction and modeling of rough surfaces are more idealized, such as rough self-affine surfaces, wave surfaces, anisotropic surfaces, etc., which ignores the stochasticity and complexity of the real engineering surfaces, and there may be a certain deviation from the microscopic flow behavior in the real rough contact interface. (2) The original surface topography inevitably plays an important role in the contact interface topography and the distribution of interfacial microchannels, so it is extremely crucial to study the dynamic evolution of the contact interface topography under stress and to establish the correlation between the original topography and the interface topography. (3) Thin fluid flow in rough contact interface is a complex gas–liquid–solid coupling problem, which depends on the shape, size, and distribution of the microchannels, and the role of surface energy needs to be considered at the same time. While the current researches for capillary-driven flow mainly focus on the effect of microchannel geometry on the flow characteristics, the fluid flow in real interface is scarcely observed

from an experimental point of view, and the effect of contact stress on the microchannel size and connectivity is rarely taken into account.

In this study, we performed the *in-situ* observations for the flow behaviors of fluid in the contact rough surfaces. The effects of surface roughness and topographical variation on the fluid flow characteristics in the contact interface were studied. The image processing method was newly proposed to analyze the topographical variation of contact surfaces, the length of interfacial microchannels and the resulting seepage flow. Further mechanics discussions provided insights for the engineering of fluid-based tribology, sealing and other mechanical systems.

2 Experimental details

2.1 Fabrication of rough rubber surfaces with different roughness

The rough rubber surfaces with different roughness are prepared through transferring the liquid PDMS (Sylgard 184 poly-dimethylsiloxane, Dow Corning, U.S.A.) on the sandpapers with different grit number (220#, 280#, 500#). The detailed preparing process is shown in Fig. 1. First, the prepolymer and curing agent were mixed at the mass ratio of 10:1 and stirred thoroughly until dense bubbles appeared, and then degassed by a vacuum pump for 0.5 h to extract all the large bubbles. After pouring the mixture into containers with different types of sandpaper molds pasted on the bottom, vacuum pumping was carried out for 2 h to extract all small air bubbles from the mixture, which was then cured in an oven at 80 °C for 8 h. Finally, the cured PDMS samples were peeled off from the sandpaper, washed with alcohol through an ultrasonic cleaner for 0.5 h to remove the impurities and stains, and cut into 8 mm × 8 mm squares as the lower specimens. The PDMS samples cured on the 200#, 280#, and 500# abrasive papers are denoted as sample A, B, C respectively.

2.2 Topography characterization of rough surfaces based on ISO 25178

The surface topography of the three PDMS samples was quantitatively characterized by using laser confocal microscope (VK-X250, Keyence, Japan) (Fig. 2). The different colored scales represent different surface heights on the samples, and the height distribution of the entire rough surface can be obtained through the rainbow colormaps. The greyscale colormaps on the right is a supplement to the measurement results of three-dimensional topography. The size of surface pits and bumps can be approximated from the scale. The skewness of topography height distribution S_{sk} was measured, which reflects the asymmetry of surface deviations about the mean plane. It is found that the surfaces of three samples exhibit negatively skewed characteristics (S_{sk}<0). And we choose four representative parameters (arithmetical mean height S_a, texture aspect ratio S_{tr}, root mean square gradient S_{dq}, valley void volume V_{vv}) from the ISO 25178-2 to quantitatively describe the morphology characteristics of the rough surfaces, which are strongly related to the interfacial

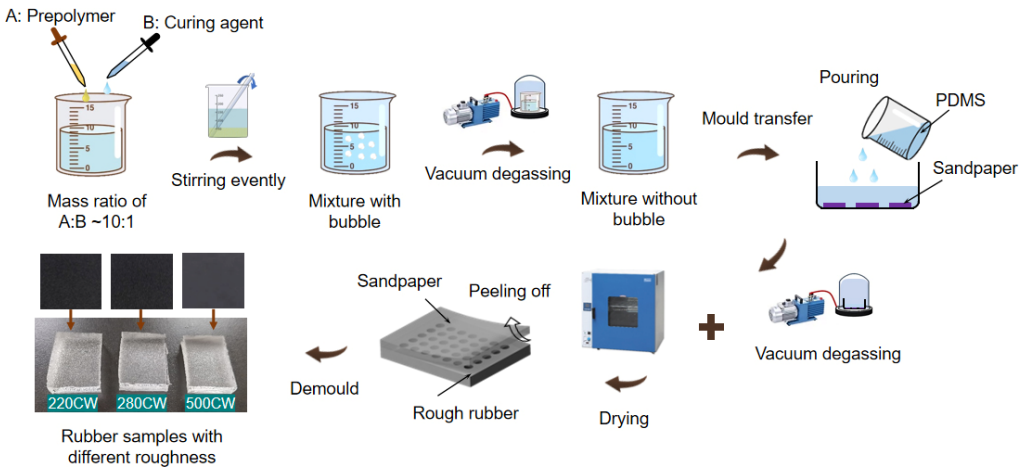

Fig. 1 Preparation of PDMS surfaces with different roughness.

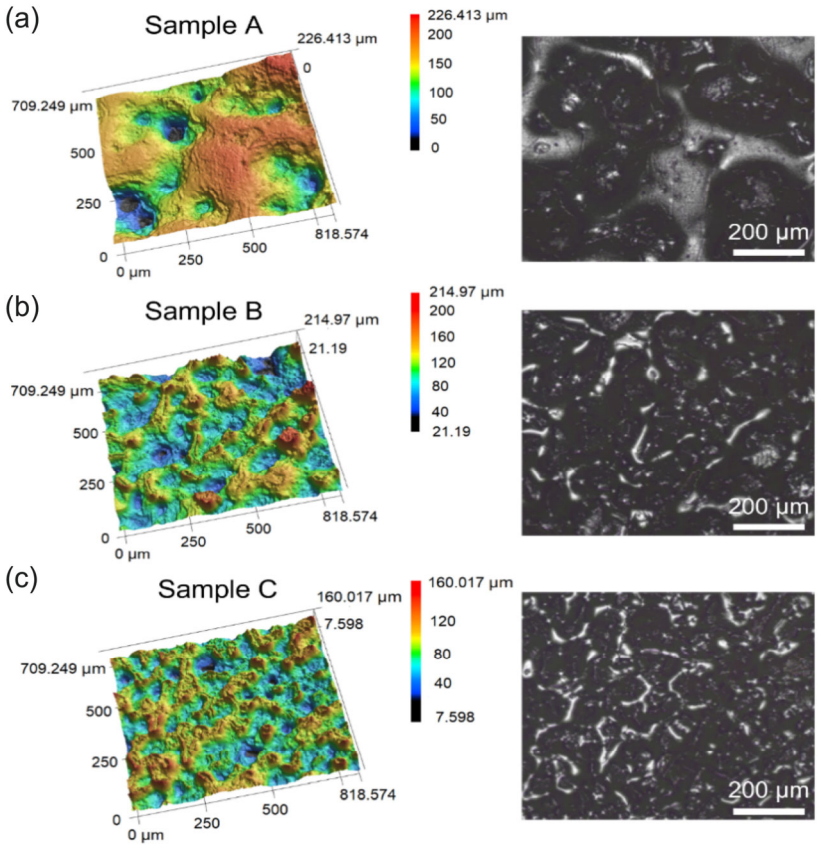

Fig. 2 3D surface topography of PDMS surfaces. (a) Sample A transferred by silicon carbide sandpaper with 220 grit. (b) Sample B transferred by silicon carbide sandpaper with 280 grit. (c) Sample C transferred by silicon carbide sandpaper with 280 grit.

flow properties (Table 1). The height parameter S_a is extended from R_a, which refers to the arithmetic average of the z-coordinate distance between the measured contour surface and the base surface within the sampling area, and is an overall measure of the surface height. It is found that the S_a of Sample A was the largest. The spatial parameter S_{tr} is used to identify the surface topography type, i.e., whether the surface has the same texture shape in any direction. The value of S_{tr} is ranging from 0 to 1. For S_{tr}>0.5, it means that the surface has a more uniform surface texture in different directions, and for S_{tr}<0.5, it means that the surface does not have a uniform surface texture in different directions. The S_{tr} values of three specimens are all greater than 0.5, indicating that although the surface is randomly rough, the texture is uniform in different directions and belongs to isotropic surface. S_{dq} is a generalized measure of the slope of a surface and contains a combination of both magnitude and spacing attributes. The flatter the surface, S_{dq} tends to 0. From Table 1, it can be seen that sample A has the smallest slope, which implies that although the overall height of the sample A is larger, the peaks and valleys are also widely spaced, so the surface is relatively flat. V_{vv} refers to the average volume of voids at bearing ratios of 80% to 100%. The larger V_{vv} is, the larger the area of voids on the surface under bearing conditions.

Table 1 3D topographic maps and topography characterization parameters of prepared samples.

3D characterization parameter	Sample		
	A	B	C
S_a (μm)	30.5	19.7	14.3
S_{tr}	0.6	0.8	0.8
S_{dq}	1.8	2.6	2.9
V_{vv} (mL/m^2)	6.7	3.0	2.2

2.3 Fluid flow test in rough contact interface

The observation of fluid was performed by using a homemade optical *in-situ* tester (Fig. 3(a)), which

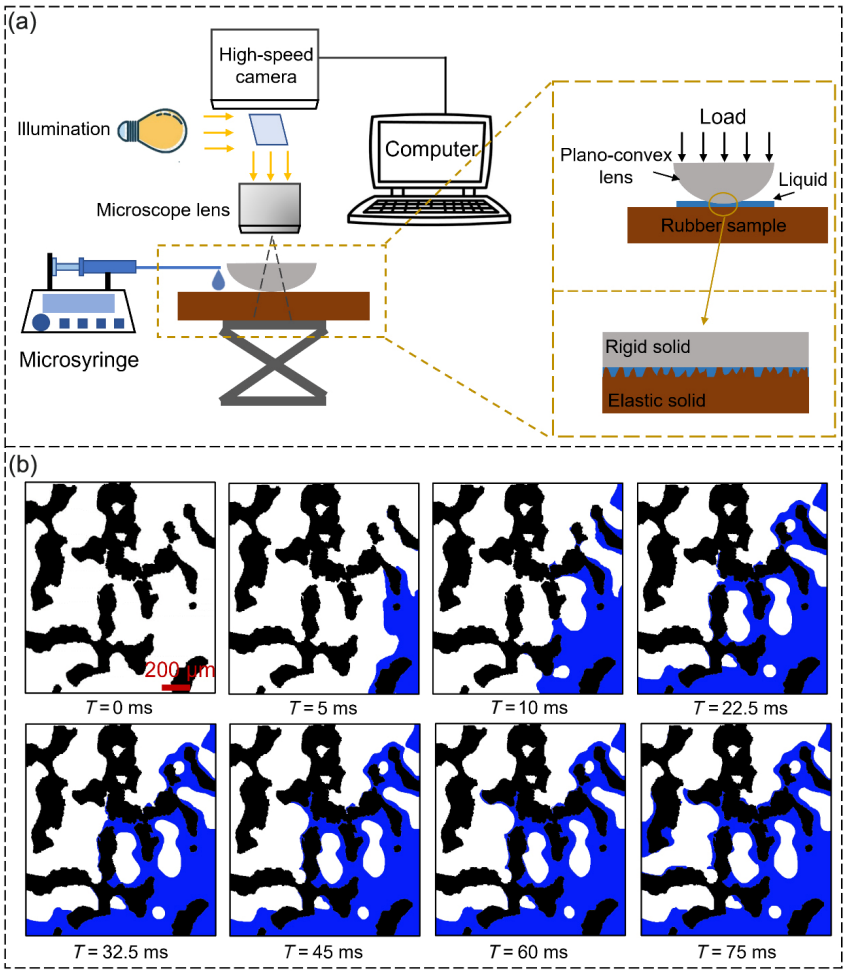

Fig. 3 Interfacial fluid flow experiments based on an optical *in situ* observation tester. (a) Schematic diagram of the tester, which consists of three main parts: optical microscope system, loading system, and microsyringe system. (b) The seepage process of liquid in the contact interface of sample A at a load of 0.3 N.

consists of motion, loading measurement, and optical microscopy systems. The PDMS samples with different roughness were chosen as the substrate contact samples. A quartz plano-convex lens with a diameter of 6.3 mm and root-mean-square average roughness < 10 nm was chosen as the counter sample. To ensure the visualization of the contact interface, the upper plano-convex lens is fixed to the L-plate with open holes, which are connected to the loading device. The PDMS sample is fixed to the linear motion module by a clamp. The displacement signals are obtained by adjusting the distance between the upper and lower sample, which could be converted into electrical signals by the capacitive displacement sensor and transmitted to the computer via a controller. The processing software enables the conversion from displacement to force so that the load can be obtained in real-time. It is noted that a 10X microscope objective equipped with a high-speed camera (Revealer M230, Hefei Fuhuang Agile Device, China) is used to observe the contact interface through the lens. The spreading process of the liquid in the contact interface is recorded at an acquisition rate of 3,000 fps after gently dripping a 3 μL drop of anhydrous ethanol at the lower right corner of the contact interfaces with a micro syringe pump (TJ-3A/W0109-1B, Longer Precision Pump Co., Ltd.). In this experiment, the body force of the liquid is ignored and the microscopic flow of the liquid under microgravity conditions is approximated. Due to the low surface energy of PDMS, anhydrous ethanol with a relatively lower surface energy (22.27 mN/m) was chosen for better observation of flowing fluid.

2.4 Extraction and quantitative characterization of interface image

To explore the effect of surface roughness on the fluid flow characteristics, the contact interface images were analyzed by using the digital image processing technique as in previous studies [21]. The snapshot images of interfacial flow obtained were the identical size of 448 × 500 pixels. The brightness scale of each snapshot image was divided into various discrete intervals from black to white. The specific gray values were used to represent different brightness intervals. The two-dimensional digital image can be produced by assigning values to each point on the image according to the interval corresponding to its brightness. Then the contact image was segmented through the optimal global thresholding technique based on the Otsu method, in which the optimal separation threshold T is calculated based on the gray value of the original image. The point in the image with a pixel value greater than T is considered the target point and the pixel value of such a point is changed to 1. The point with a gray value less than or equal to T is the background point and the pixel value of such a point is changed to 0. In this way, the original image is transformed into a binary image, where a pixel value of 1 is a white point representing the void region (i.e., the microchannel) and the pixel value of 0 is a black point representing the contact region. Fluid flow in the interface at different moments can also be extracted according to the above-mentioned method and is indicated in blue color. When the fluid flows along the contact interface, the edge of the liquid is constantly moving and we need to confirm the precise position of moving boundary through repeatedly comparing images from adjacent moments. Then the boundary of liquid filling area could be extracted from the image and marked with blue part. In addition, it is known that the liquid could not infiltrate into the real contact area, and we finally need to remove the real contact area under dry condition in the wetting blue part so that the fluid-filled area is obtained. The liquid spreading with time in the interface of sample A at the load of 0.3 N is shown in Fig. 3(b). With the increase of time, the liquid spreading area increases, but the spreading speed slows down gradually. The detailed flow process will be analyzed in the following section.

3 Results and discussion

3.1 Feature length and distribution of the microchannels

Due to the low Reynolds number of fluid and the small thickness of the fluid film, the fluid pressure does not affect the topographical variation of contact interface [10]. Therefore, the size and distribution of microchannels are the main factors for the flow behavior of the liquid in the rough contact interface. To analyze the size and distribution of the microchannels and their influence on the dynamic topography variation of contact interface, the Monte Carlo algorithm was introduced to investigate the feature lengths and distribution of the microchannels [22, 23] (Fig. 4). The variation curves of the feature lengths with the load and the correlation characteristics with the 3D topography parameters can be investigated by this method. The main principle of the algorithm is to randomly place a square with side length L on the binary image of the contact interface and calculate the area of the contact region in the square. By constantly changing the length of the square, the maximum square length of the square is calculated when the contact area in a randomly placed square is most likely to be zero, which is the feature-length of the microchannel. In this paper, squares of each size are randomly placed onto the image in a repeated run of 20,000 times to ensure the accuracy and reliability of the final measured microchannel feature lengths, for which the area of the contact regions and the occurrences appearing in the square are counted and presented as a histogram. The computational process of the Monte Carlo algorithm is explained in detail through an example below.

Top left of Fig. 4 shows the binary image of the contact interface of sample A at a normal load of 0.3 N. When the square length is 500 μm, the most probable number of black pixels per square (M) is 11,472 and the number of occurrences of zero black pixel per square (N) is 0, which implies that the square intersects with the contact region each time and the square length is greater than the feature length of microchannels. Similarly, when the square length is 350 μm, M is 4,170 and N is 0, indicating that the feature length of the microchannels is less than 350 μm.

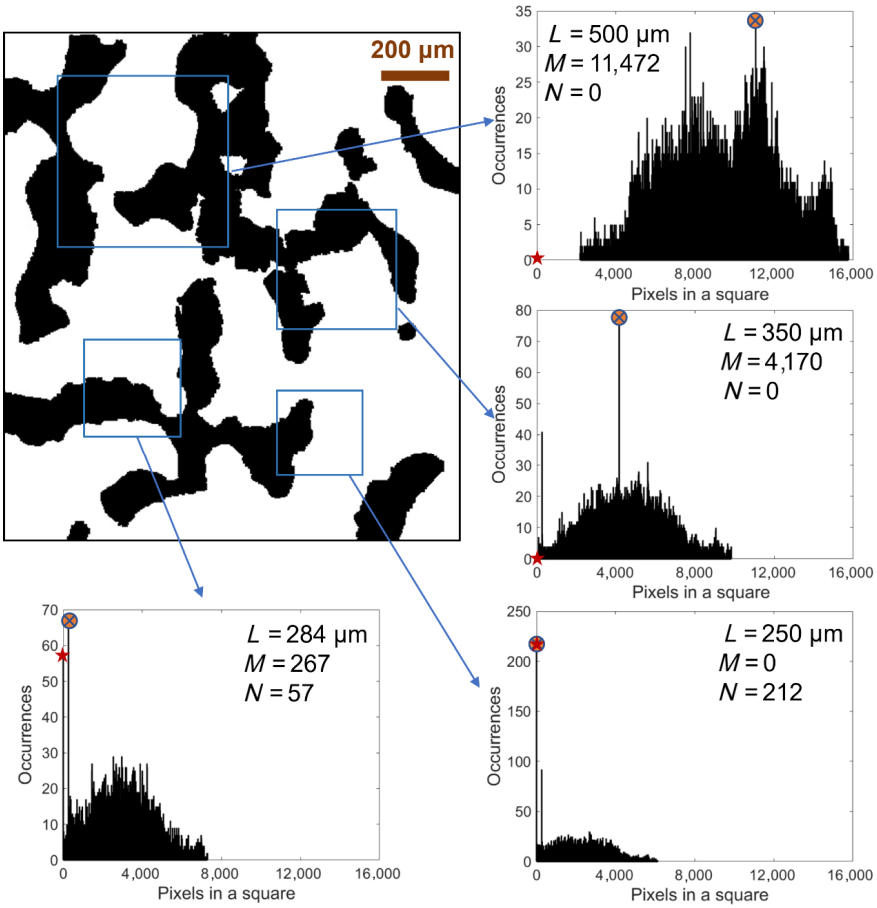

Fig. 4 Schematic diagram of Monte Carlo-based algorithm for solving the feature length of interfacial microchannels.

When the square length is 250 μm, M is 0 and N is 212, which indicates that there are many occurrences of squares that do not intersect with the contact area, and the feature length of the microchannel is not less than 250 μm. Therefore, when N is 0, the larger M is, the square length deviates positively from the feature length, and when M is 0, the larger N is, the square length deviates negatively from the feature length. It is shown that when M and N are both smaller and close to 0, the square length is equal to the microchannel characteristic length. The characteristic length of the microchannel in this contact state is 284 ± 6 μm, which is averaged from the total 20,000 cycles of simulations.

By extracting the probability of zero black pixels in the square box with different lengths, we could obtain the distribution of microchannels in the interfacial binary image. It can be found that as the square length gradually increases, the number of occurrences of zero black pixels intersecting with the square decreases as shown in Fig. 4. The probability of the event is calculated by dividing the number of occurrences into the total number of 20,000 iterative cycles. A comparative analysis shows that the probability of zero black pixel in the square box varies with different contact states of sample A (Fig. 5(a)). The smaller the normal load, the higher the probability of zero black pixel in the same size square, which means the larger the microchannel size. The stars in the figure represent the feature length of the microchannel under different working conditions, and by enlarging the local area in Fig. 5(a), it can be found that when the square length is equal to the feature length of the microchannel, the probability of the zero black pixels is less than 0.01 (Fig. 5(b)). This suggests that the feature length of the microchannel obtained by the Monte Carlo algorithm is the maximum square length where the zero black pixels in a randomly placed square is most likely to appear, which verifies the accuracy of our method.

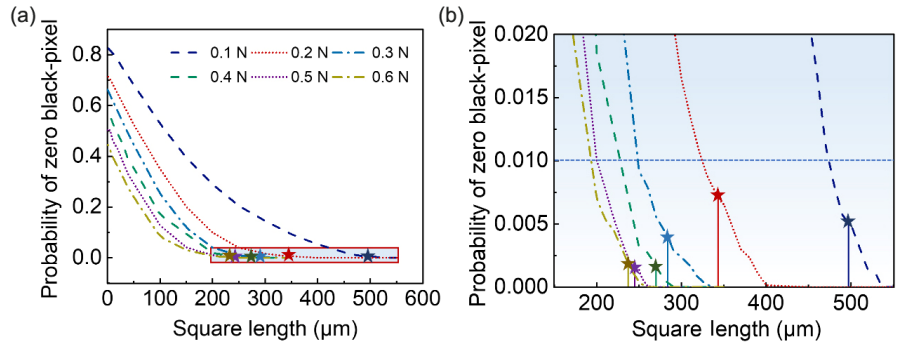

Fig. 5 Distribution of interfacial microchannels characterized based on Monte Carlo algorithms. (a) The effect of normal load on the probability of zero black-pixel. (b) Enlarging the local area of microchannel feature length in (a).

We computed the feature length of different sample surfaces under various loads using the Monte Carlo algorithm (Fig. 6), and the calculation results show that the feature length of microchannels gradually decreases with the increase of contact pressure, and the size of microchannels is inversely proportional to the load (Fig. 6(a)). Additionally, the feature length of the interfacial channels of sample A is the largest and that of sample C is the smallest under the same load. For example, under the lower load (0.1 N), the microchannel feature length of sample A (500 μm) is much larger than that of sample C (220 μm). It is worth noting that surface topography and roughness also have an obvious influence on the size and distribution of microchannels in the contact interface. Based on the 3D topographic parameter system (ISO 25178), three typical parameters (S_a, V_{vv}, S_{dq}) are selected to characterize the rough surface. The correlation between the microchannel feature lengths and these topographic parameters is established (Figs. 6(b)–6(d)). It can be seen that the microchannel size is positively correlated with S_a and V_{vv}, and negatively correlated with S_{dq}. For the prepared surfaces with isotropic topography, their arithmetic mean height would increase with the greater spacing of surface peaks. The line roughness of the sample A and the sample C are extracted, and it can be concluded that the transverse size of the microchannels is strongly correlated with the spacing of the peaks, therefore the surface with greater roughness has a

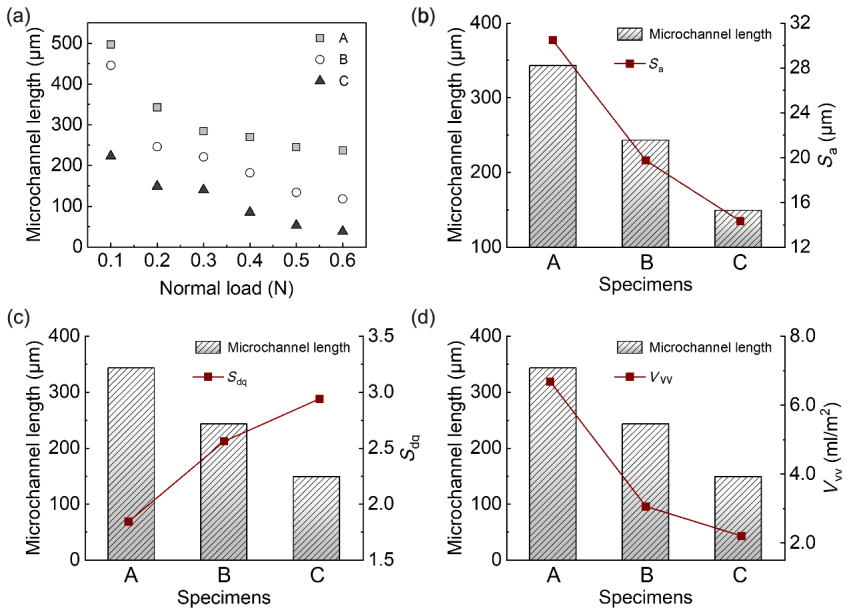

Fig. 6 (a) Curves of interfacial microchannel feature length versus load. (b) Correlation between microchannel feature lengths and S_a. (c) Correlation between microchannel feature lengths and S_{dq}. (d) Correlation between microchannel feature lengths and V_{vv}.

larger microchannel size under the same load (Fig. 7, ①②>③④⑤). And the microchannels are similar to V-shaped valleys in the longitudinal cross-section. The depth of the channels is not uniform, with smaller depth near the solid contact region and larger channel depth away from the solid contact region.

3.2 Interacting characteristics of contact surfaces

The interacting characteristics of contact surfaces can be described by using the mechanical-rheological model (Fig. 8). Based on this model, the rough contact interfaces could be categorized into three regions including the contact regions, the open void regions, and closed void regions [24]. The open void regions can form the interfacial microchannels, which enables that the liquid could only spread along the open void regions. The closed void region refers to the part of the void region that is not connected to

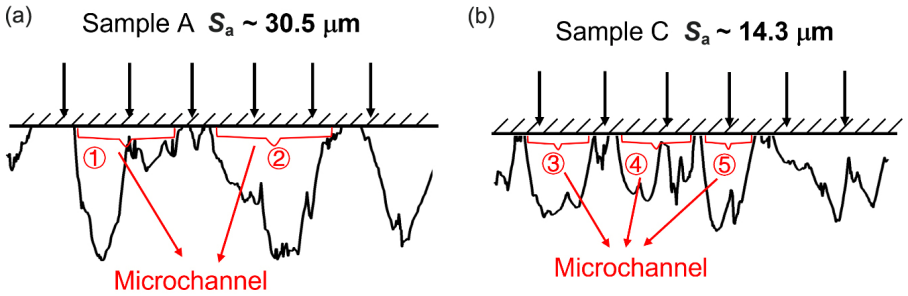

Fig. 7 Diagram of microchannels in the interface with different roughness (a) S_a ~ 30.5 μm and (b) S_a ~ 14.3 μm under the same load.

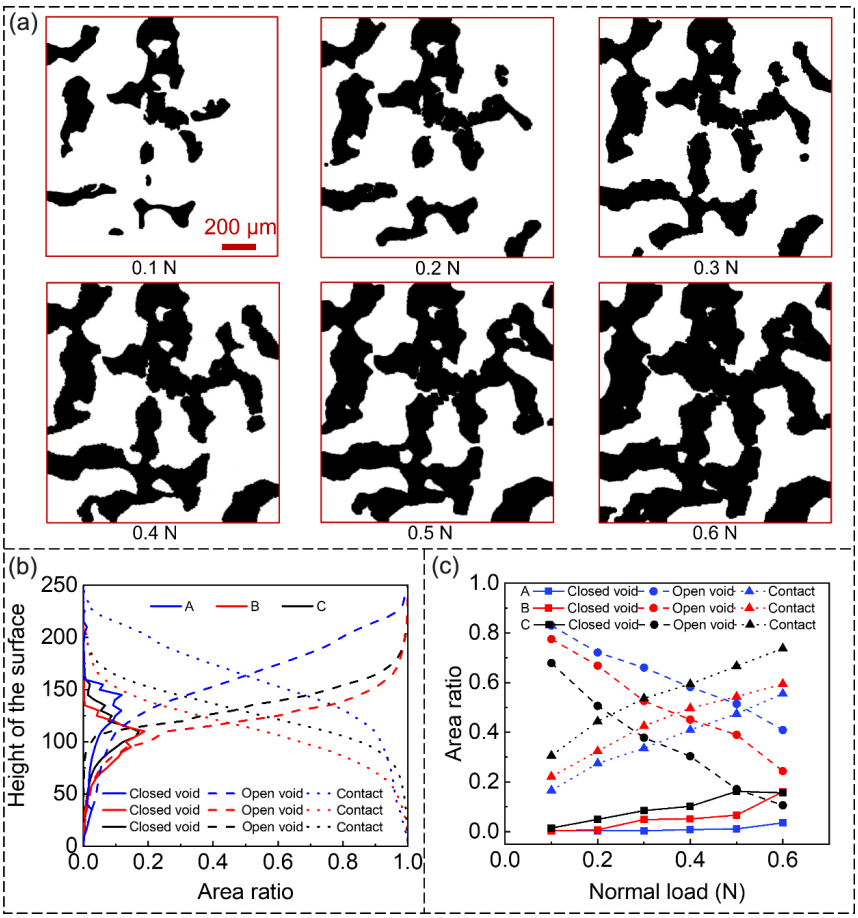

Fig. 8 Quantitative characterization of interfacial morphological properties. (a) Static binary images of sample A under different loads. (b) Mechanical rheological curves. (c) Variation curve of area ratio with load.

the interface boundary. As the closed void region is not connected to the external boundary, the liquid cannot infiltrate into the closed void region and only spread along the open void region. Therefore, it is supposed that the interfacial flow behavior is dominated by the open void regions near the contact surfaces. Figure 8(a) shows the binary contact image of sample A under different loads. It was shown that when the applied load is small, the interface topography mainly consists of solid contact regions and open void regions with the relatively smaller closed void regions. As the load increases, the contact area gradually increases and merges, and some open void regions are replaced by contact regions and closed void regions. Numerical analysis is used to extract the number of black pixels and white pixels in the whole image and calculate their ratio to the total number of pixels. The ratios of the black pixels and white pixels are the ratios of the contact area and the void area to the total area, respectively. The mechanical-rheological curves of different surfaces are obtained by calculating the contact area ratio, the closed void area ratio, and the open void area ratio of the interacting surfaces at different heights (i.e., different contact stresses). In order to standardize uniformity and facilitate comparison, the true height of the surface is converted into the gray value of [0, 255]. The height values of the converted surfaces are all in the interval from 0 to 255. That is, the highest point on each of the three surfaces has a height value of 255 and the lowest point has a height value of 0. The images with different gray values can be equivalent to the contact interface images under different loads. The image with gray value 255 refers to the situation when the upper surface is just in contact with the highest point of the lower surface, which is equivalent to the contact image when the load is 0. And the image with gray value 0 is equivalent to the image when the two interacting surfaces are in full contact. The "Height of the surface" parameter in Fig. 8(b) is actually a gray scale value, representing the situation when the upper surface comes into contact with different height points on the lower surface under different stresses. It can be seen that the solid contact area becomes larger, the open void area gradually decreases and the closed void area first increases and then decreases with the increase of the contact stress (Fig. 8(b)). When the contact stress of the two surfaces is 0, it can be considered that the whole surface is a void region. As the load increases, the two interacting surfaces ideally turn into complete contact from partial contact with near-zeroed void area formed in the interface. In addition, the variation of area ratio versus the normal load is obtained through real contact interface images under different loads (Fig. 8(c)). The contact area ratio of sample C is the largest and the void area ratio of Sample A is the largest under the same load.

3.3 Fluid flow process and flow path in rough contact interface

The fluid flow between the contact interface under different loads is shown in Fig. 9 and Movie S1 in the Electronic Supplementary Material (ESM), where the black part is the contact area and the colored parts are marked to represent the fluid that infiltrates at different moments. The microchannel shape in the contact interface is randomly irregular, due to the distribution of contact regions, which resulted in the strongest flow ability for sample A under the comparable load conditions (Movie S2 in the ESM). For sample A, the distribution of the contact region is presented as large and sparse, while it is small and dense in sample C. Interestingly, during the fluid spreading along the contact interface, we found that a kind of "trapped air" phenomenon (marked by the red dotted line), which suggested that not all gases would be completely replaced by the infiltrating liquid during the process of liquid infiltration in the non-contact zone. The main reason for this phenomenon is that the microchannels at the interface have some longitudinal depth with different scales, and those microchannels with larger longitudinal depth could not be completely filled by the liquid, which results in the formation of "trapped air". Notably, the distribution of air pockets within the contact interface of sample A is relatively sparse (Fig. 9(a), air trap ①), and the air pockets in the contact interface of sample C are small and dense (Fig. 9(c), air trap ⑥), which is highly related to the original surface morphology. For the same rough surface, the area of air pockets increases gradually with the increase of load (Fig. 9(a), air trap ①→②→

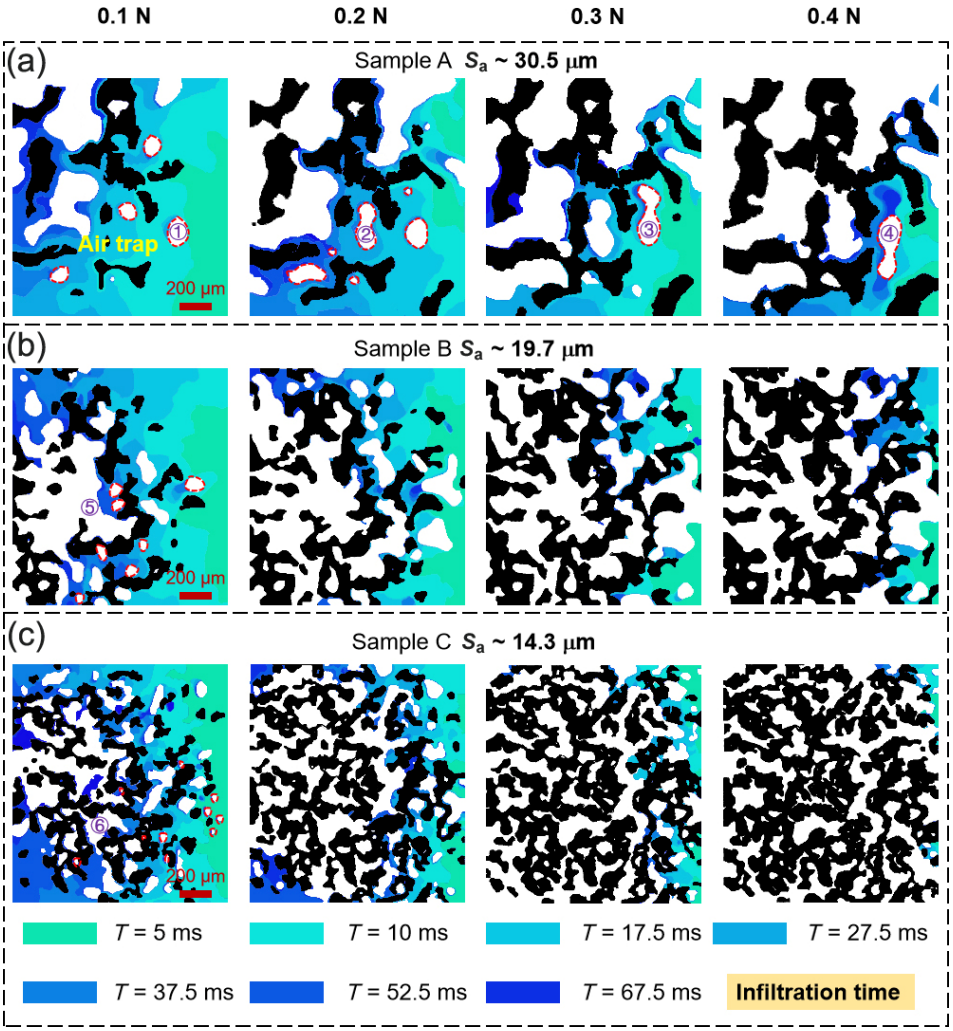

Fig. 9 Fluid flow images in the rough contact interface with different surface roughness (a) S_a ~ 30.5 μm, (b) S_a ~ 19.7 μm, (c) S_a ~ 14.3 μm and different loads (0.1 N, 0.2 N, 0.3 N, 0.4 N), where different colors represent the liquid seepage at different moments.

③→④). It is mainly because the contact area increases and the size of the microchannels decreases (including transverse and longitudinal dimensions) as the contact stress increases. The solid–gas and solid–liquid interfacial tensions are strongly affected by the channel size [25], so the area of air pockets increases with increasing load.

The non-uniformity of microchannel depth not only leads to "trapped air" phenomenon, but also affects the flow rate of the liquid in the interface. It is defined that the spread area ratio refers to the area of liquid compared to the total observation area and the spreading rate is the ratio of the spreading area that grows per unit of time. It can be seen that the spreading area ratio and spreading rate are negatively correlated with the load (Figs. 10(a) and 10(b), Movie S1). The spreading rate of the liquid in the interface decreases with time, the fastest spreading rate at the initial moment, and finally tends to 0. Moreover, the surface roughness also affects the fluid flow properties (Fig. 10(c), Movie S2). The larger the original surface roughness, the larger the fluid spreading area and spreading rate under the same contact load. Finally, we established the correlation between the feature length of the microchannels and the spreading area of the liquid at a certain moment (T = 75 ms) (Fig. 10(d)). And the results show that for the same original surface, the larger the size of the microchannel is, the larger the area of the liquid spread inside the interface at the same moment is. While for different surfaces, it does not present such a monotonic relationship and the spreading area is not necessarily larger when the

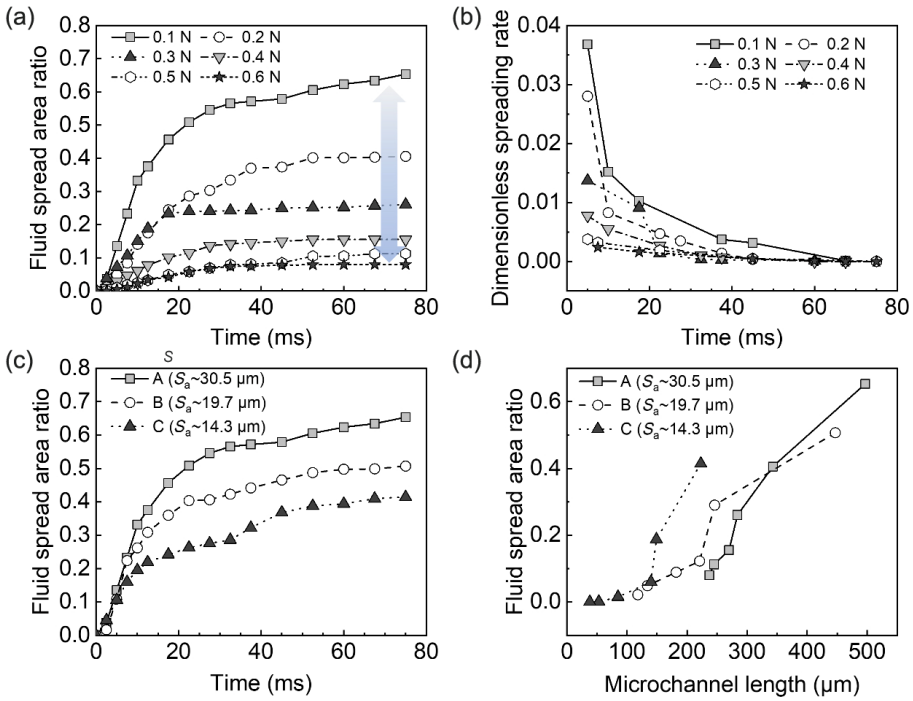

Fig. 10 Quantitative characterization of fluid behavior. (a) Curves of Fluid spreading area ratio with time and load. (b) Curves of fluid spreading rate with time and load. (c) Effect of surface topography on interfacial fluid spreading area. (d) Correlation between spreading area and feature length of microchannels.

size of the microchannel is larger, which is greatly related to the shape and depth of the microchannels. It should be pointed out that due to the limited ability and technology, the feature length of microchannels in present work is only a quantitative characterization of the channel cross-section, which could not reflect the depth characteristics of the microchannels, and the depth of the channel also has a great influence on the spreading of the liquid, which is also required to be improved in the subsequent studies.

The fluid flow in the rough contact interface seems to be random and disordered, but there is still a certain law to follow. The liquid spreading in the contact interface of the sample A when the load is 0.2 N is analyzed (Fig. 11), where the yellow arrows indicate the flow direction. In conventional thinking, we imagine that the liquid should spread forward along the large-sized microchannels, while the experimental results show that the liquid tends to flow toward the contact region after infiltrating from the boundary of the contact interface, and then it spreads along the solid wall and flows toward the void region in the end. It is interestingly found that the void region with a larger area is prone to inducing the occurrence of "trapped air". Since the original rough surface is composed of randomly distributed irregular micro convex bodies and micropits, the depth of void region is uneven when two rough surfaces contact with each other. The depth of the microchannel close to the contact region is small and that away from the contact area is large (Fig. 7). The existence of irregular microchannel increases the flow resistance. The instability and variation of solid–gas and solid–liquid interfacial tensions are caused by the surface heterogeneity near the contact line [25, 26]. Therefore, the driving force changes as the liquid flows to the region of greater depth and cannot squeeze out all of the gas in it. Liquid wraps around the gas and forms an air pocket [27].

To clearly analyze the fluid flow process and flow path in rough contact interface, the local region of interface is amplified (Fig. 12). It is seen that each contact region could be regarded as a self-island, and the irregular gaps between adjacent islands are the microchannels, which get smaller and smaller as they get closer to the island. The shape of the channel is similar to a wedge (marked by dashed line), in which the part near the contact region corresponds to

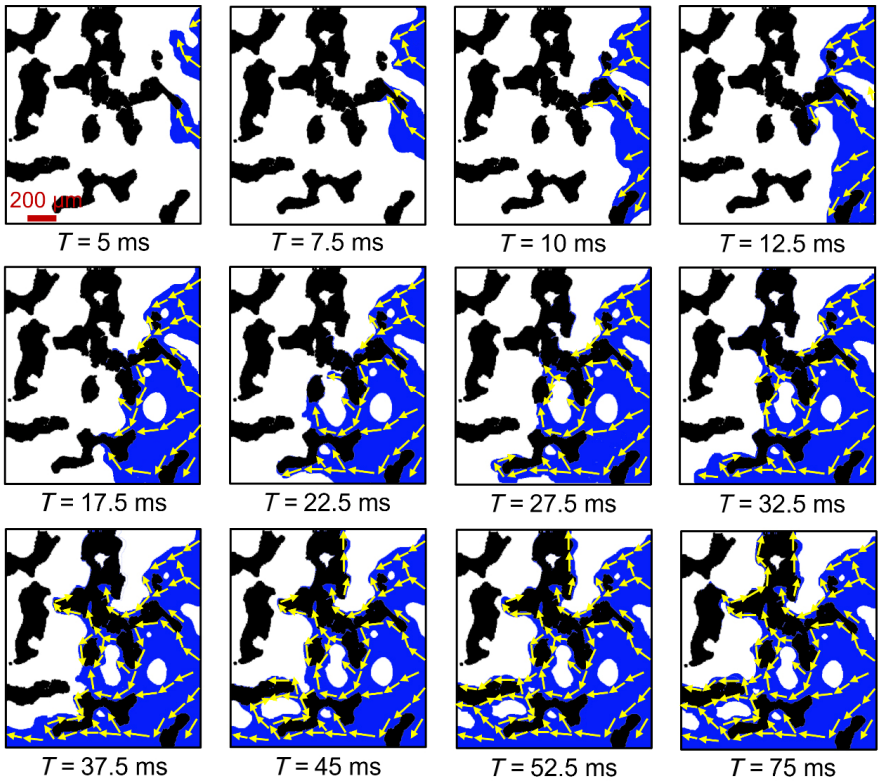

Fig. 11 Spreading path of the liquid in the contact interface of sample A at a load of 0.2 N. The arrows represent the direction of fluid flow.

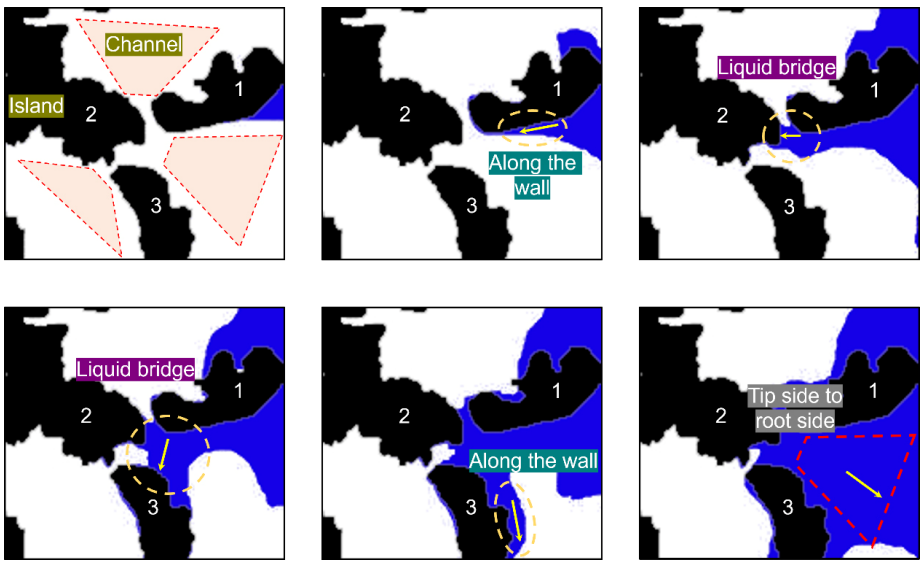

Fig. 12 Localized enlarged schematic of liquid spreading in the interface.

the tip side of the wedge channel. According to the Young–Laplace equation, the liquid tends to move from the tip side to the root side in the hydrophilic wedge channel, so the liquid does not directly spread along the void region. It is worth noting that the spreading path of the liquid is divided into several parts. Firstly, it flows from the inlet to one of the islands and spreads around the island wall. When flowing to the place where the gap between two neighboring islands is small, it quickly connects the two islands in the form of a liquid bridge. The flow then spreads from the tip side to the root side of the

wedge channel along the direction of the Laplace pressure difference.

3.4 Mechanical analysis of liquid flow in contact interfaces

The fluid is subjected to capillary driving force and adhesive resistance of the solid walls. Since the microchannel is formed by a glass lens and a rough rubber viscoelastomer under a certain contact stress, the liquid in the microchannel will be in contact with the four solid walls, in which the top of the microchannel is approximated to a flat surface and the other three surfaces are rough rubber surfaces, and the driving force is derived from the surface tension of the moving contact line. The flow behavior within the capillary microchannel of the real rough contact interface is very complex. In order to analyze the driving force, the microscopic flow behavior of the liquid in a short period of time is approximated as a steady state flow based on the quasi-steady state assumption [17], that is, the angle between the gas/liquid interface and the upper wall surface is always the steady-state contact angle θ_x and the angle between the gas/liquid interface and other surfaces is always θ_y. The irregular microchannels are equated to a number of rectangular capillaries with different lengths and the contact line between the liquid and the microchannel is divided into four parts.

The moving contact line in the cross-section is shown schematically in Fig. 13(a). The left and right surfaces of the microchannel are curves with shape function $w_l(x)$ and $w_r(x)$, respectively. The radius of curvature of the gas/liquid interface can be calculated according to the geometric relationship under the quasi-steady state condition in Eq. (1).

$$R_1 = \frac{w_r}{2\cos\left(\theta_y + \dfrac{\arctan w_l'(x) - \arctan w_r'(x)}{2}\right)} \tag{1}$$

The surface tension is along the tangential direction of the gas/liquid interface, and since the component in the vertical direction is balanced with the gravity of the liquid, only the horizontal component is considered. According to the Young–Laplace equation [17], the component of the surface tension coefficient along the horizontal flow direction is in Eq. (2).

$$F_\gamma = \frac{\gamma_{lg}}{R_1} \cdot w_r \tag{2}$$

where the γ_{lg} refers to the surface tension of liquid–gas interface, for the present work, it is about 22.27 mN/m (anhydrous ethanol).

The length of contact line is in Eq. (3):

$$l_1 = R_1 \cdot \left\{180° - 2\theta_y - \left[\arctan w_l'(x) - \arctan w_r'(x)\right]\right\} \cdot \pi / 180 \tag{3}$$

The surface tension in the horizontal direction can

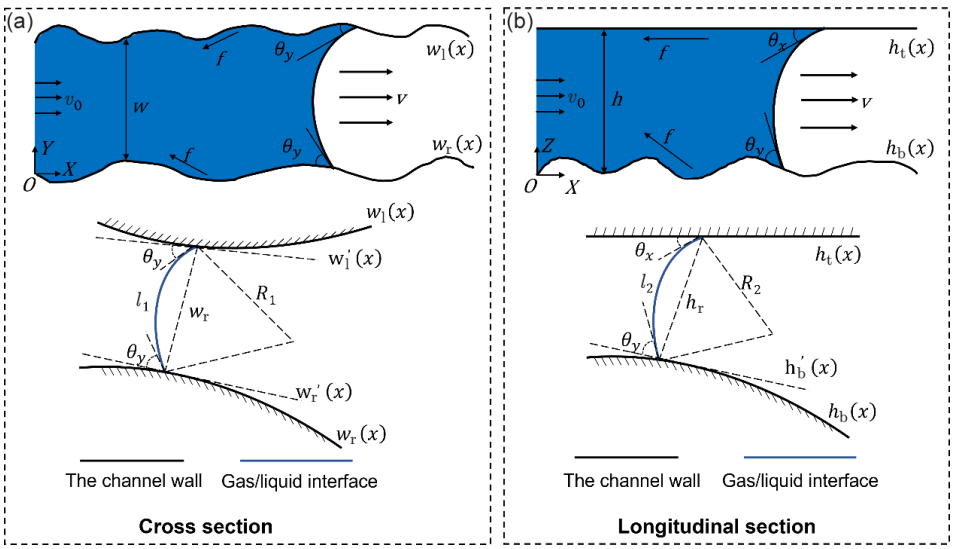

Fig. 13 Schematic diagram of surface tension derivation. (a) The moving contact line in the cross-section. (b)The moving contact line in the longitudinal section.

be obtained in Eq. (4):

$$F = F_\gamma \cdot l_1 = \gamma_{\mathrm{lg}} \cdot w_{\mathrm{r}} \cdot \left\{180° - 2\theta_y - \left[\arctan w_{\mathrm{l}}'(x) - \arctan w_{\mathrm{r}}'(x)\right]\right\} \cdot \pi / 180 \tag{4}$$

The moving contact line of the liquid in the longitudinal section is shown schematically in Fig. 13(b). The top and bottom surfaces of the microchannel are curves with shape function $h_{\mathrm{t}}(x)$ and $h_{\mathrm{b}}(x)$, respectively. The radius of curvature of the gas/liquid interface can be calculated according to the geometric relationship in Eq. (5).

$$R_2 = \frac{h_{\mathrm{r}}}{2\cos\left(\dfrac{\theta_x + \theta_y}{2} - \dfrac{\arctan h_{\mathrm{b}}'(x)}{2}\right)} \tag{5}$$

The component of the surface tension coefficient along the horizontal flow direction is in Eq. (6).

$$F_\gamma = \frac{\gamma_{\mathrm{lg}}}{R_2} \cdot h_{\mathrm{r}} \tag{6}$$

The length of contact line is in Eq. (7).

$$l_2 = R_2 \cdot \left[180° + \arctan h_{\mathrm{b}}'(x) - \theta_x - \theta_y\right] \cdot \pi / 180 \tag{7}$$

The surface tension in the horizontal direction can be obtained in Eq. (8):

$$F = F_\gamma \cdot l_2 = \gamma_{\mathrm{lg}} \cdot h_{\mathrm{r}} \cdot \left[180° + \arctan h_{\mathrm{b}}'(x) - \theta_x - \theta_y\right] \cdot \pi / 180 \tag{8}$$

The theoretical results (Eqs. (4) and (8)) show that the capillary driving force is related to various factors, such as surface wettability, microchannel size (width and depth), and microchannel shape. It is noted that the size and shape of the microchannel are determined by the contact stress and surface morphology. From the final derived equation (Eq. (8)), it can be seen that the driving force is proportional to the width and depth of the channel, so that the greater the contact load, the less capillary driving force. In addition, according to the previous study [17], the adhesive resistance of the solid wall to the fluid could be obtained in Eq. (9):

$$F_\mu = 12\mu V_0 h_0 \int_0^L \frac{1}{h^2}\,\mathrm{d}x \tag{9}$$

where μ is the dynamic viscosity of the fluid, h is the difference between the shape function of the top surface and the bottom surface, L represents the spreading length of the fluid in microchannel, V_0 and h_0 are the fluid velocity and the height of the flow channel at the inlet, respectively. It can be seen that the adhesive resistance of the fluid is mainly related to the nature of the fluid and the microchannel depth, and it is inversely proportional to the microchannel depth. For the actual observation, liquid spreading ability is stronger when the load is smaller, which indicates that the real situation is consistent with the equations for driving force and resistance. Moreover, the width and depth of microchannels increase with surface roughness with respect to different rough surfaces under the same load, and thus the best flow performance is achieved for sample A.

4 Conclusions

This study investigates the dynamic topography variation and fluid flow characteristics in rough contact interface formed between the rough PDMS surface and plano-convex lens, and the following conclusions can be drawn.

1) The Monte Carlo algorithm and the mechanical rheological model could effectively quantitatively characterize the mechanical rheological properties of the contact interface as well as the size and distribution of the microchannels. It is found that both the original 3D surface morphology and the contact stress have a great influence on the contact state and interface topography. As the load increases, the contact area increases and the open void area gradually decreases, while the closed void area first increases and then decreases. The feature length of the microchannel is inversely proportional to the load and root-mean-square gradient S_{dq}, positively correlated with both the arithmetical mean height S_{a} and the valley void volume V_{vv}.

2) Both contact stress and rough surface topography play a significant role in the flow properties of the liquid in the interface. "Trapped air" phenomenon occurs in the spreading process. The gas is wrapped

up in the interface by the liquid, resulting in the formation of air pockets. "Trapped air" phenomenon has a close relationship with the original surface topography. The distribution of air pockets in the contact interface of sample A is relatively sparse, which in the contact interface of sample C is small and dense.

3) The liquid tends to flow towards the contact region after infiltrating from the open void region at the boundary of the contact interface. After contacting with the solid, it spreads along the island wall and diffuses into the void region, while the region with a large void area is prone to the occurrence of air pockets.

4) The capillary driving force of the liquid in the contact interface is associated with the surface wetting characteristics, the size of the microchannels, and the gradient of the solid surface at the gas/liquid interface. The size of the microchannels and the gradient of the solid surface are dominated by the contact stresses and the surface topography.

Acknowledgements

This work was supported by the National Natural Science Foundation of China (Nos. 52375178, 52305188, 51975174, 51875153, and 51805508) and the Natural Science Foundation of Anhui Province (Nos. 2308085ME158 and 2308085QE156).

Declaration of competing interest

The authors have no competing interests to declare that are relevant to the content of this article.

Electronic Supplementary Material: Movie S1: Fluid flow in rough contact interface under different loads (MP4) and Movie S2: Fluid flow in rough contact interface with different roughness (MP4) are available in the online version of this article at https://doi.org/10.1007/s40544-024-0911-6.

Open Access This article is licensed under a Creative Commons Attribution 4.0 International License, which permits use, sharing, adaptation, distribution and reproduction in any medium or format, as long as you give appropriate credit to the original author(s) and the source, provide a link to the Creative Commons licence, and indicate if changes were made.

The images or other third party material in this article are included in the article's Creative Commons licence, unless indicated otherwise in a credit line to the material. If material is not included in the article's Creative Commons licence and your intended use is not permitted by statutory regulation or exceeds the permitted use, you will need to obtain permission directly from the copyright holder.

To view a copy of this licence, visit http://creativecommons.org/licenses/by/4.0/.

References

[1] Stupkiewicz S, Marciniszyn A. Elastohydrodynamic lubrication and finite configuration changes in reciprocating elastomeric seals. *Tribol Int* **42**(5): 615–627 (2009)

[2] Sahlin F, Larsson R, Almqvist A, Lugt P M, Marklund P. A mixed lubrication model incorporating measured surface topography. Part 1: Theory of flow factors. *Proc Inst Mech Eng Part J J Eng Tribol* **224**(4): 335–351 (2010)

[3] Narayanamurthy V, Jeroish Z E, Bhuvaneshwari K S, Bayat P, Premkumar R, Samsuri F, Yusoff M M. Advances in passively driven microfluidics and lab-on-chip devices: A comprehensive literature review and patent analysis. *RSC Adv* **10**(20): 11652–11680 (2020)

[4] Schultz R, Skoumal R J, Brudzinski M R, Eaton D, Baptie B, Ellsworth W. Hydraulic fracturing-induced seismicity. *Rev Geophys* **58**(3): e2019RG000695 (2020)

[5] Cai J C, Jin T X, Kou J S, Zou S M, Xiao J F, Meng Q B. Lucas–washburn equation-based modeling of capillary-driven flow in porous systems. *Langmuir* **37**(5): 1623–1636 (2021)

[6] Paggi M, He Q C. Evolution of the free volume between rough surfaces in contact. *Wear* **336–337**: 86–95 (2015)

[7] Persson B J. Fluid dynamics at the interface between contacting elastic solids with randomly rough surfaces. *J Phys*: *Condens Matter* **22**(26): 265004 (2010)

[8] Dapp W B, Lücke A, Persson B N J, Müser M H. Self-affine elastic contacts: Percolation and leakage. *Phys Rev Lett* **108**(24): 244301 (2012)

[9] Shvarts A G, Yastrebov V A. Fluid flow across a wavy channel brought in contact. *Tribol Int* **126**: 116–126 (2018)

[10] Shvarts A G, Vignollet J, Yastrebov V A. Computational framework for monolithic coupling for thin fluid flow in contact interfaces. *Comput Meth Appl Mech Eng* **379**: 113738 (2021)

[11] Huang D, Yan X, Larsson R, Almqvist A. The critical pressure for bulk leakage of non-planar smooth surfaces. *Tribol Lett* **70**(3): 74 (2022)
[12] Huang D, Yan X, Larsson R, Almqvist A. Leakage threshold of a saddle point. *Tribol Lett* **71**(2): 40 (2023)
[13] Cai J C, Chen Y, Liu Y, Li S, Sun C H. Capillary imbibition and flow of wetting liquid in irregular capillaries: A 100-year review. *Adv Colloid Interface Sci* **304**: 102654 (2022)
[14] Lucas R. The time law of the capillary rise of liquids. *Kolloid-Zeitschrift* **23**(1): 15–22 (1918)
[15] Washburn E W. The dynamics of capillary flow. *Phys Rev* **17**(3): 273–283 (1921)
[16] Zhu Y, Petkovic-Duran K. Capillary flow in microchannels. *Microfluid Nanofluid* **8**(2): 275–282 (2010)
[17] Zhong H, Huang W F, Li Y, Tong H, Liu G D, Wang Z Q. Flow modeling and experimental verification of flow resistors used in microfluidic chips driven by capillary force. *J Micromech Microeng* **30**(11): 115015 (2020)
[18] Pasias D, Passos A, Constantinides G, Balabani S, Kaliviotis E. Surface tension driven flow of blood in a rectangular microfluidic channel: Effect of erythrocyte aggregation. *Phys Fluids* **32**(7): 071903 (2020)
[19] Papadimitriou V A, Segerink L I, van den Berg A, Eijkel J C T. 3D capillary stop valves for versatile patterning inside microfluidic chips. *Anal Chim Acta* **1000**: 232–238 (2018)
[20] Wang J J, Salama A, Kou J S. Experimental and numerical analysis of imbibition processes in a corrugated capillary tube. *Capillarity* **5**(5): 83–90 (2022)
[21] Joshi M A. *Digital Image Processing: An Algorithmic Approach*. Delhi (India): PHI Learning Pvt. Ltd., 2018.
[22] Khare H S, Burris D L. A quantitative method for measuring nanocomposite dispersion. *Polymer* **51**(3): 719–729 (2010)
[23] Sun W, Liu X J, Liu K, Xu J M, Lu Y X, Ye J X. Mechanochemical functionality of graphene additives in ultralow wear polytetrafluoroethylene composites. *Carbon* **184**: 312–321 (2021)
[24] Pfestorf M, Engel U, Geiger M. Three-dimensional characterization of surfaces for sheet metal forming. *Wear* **216**(2): 244–250 (1998)
[25] Xian Z K, Du Z H, Chen Y F, Liu L M, You H. Dynamic contact angle measurement of hydrophilic open microchannels: The role of surface wettability. *Phys Fluids* **35**(9): 092110 (2023)
[26] Gervais L, Hitzbleck M, Delamarche E. Capillary-driven multiparametric microfluidic chips for one-step immunoassays. *Biosens Bioelectron* **27**(1): 64–70 (2011)
[27] Qin Z P, Du Z H, Xian Z K, You H. Theoretical and experimental study on capillary flow in a grooved microchannel with hydrophilic or hydrophobic walls. *J Fluids Struct* **123**: 103988 (2023)

Jiawei JI. She received her bachelor and M.S. degrees in mechanical engineering from Hefei University of Technology, Hefei, China, in 2014 and 2017, respectively. Now, she is a Ph.D. candidate in mechanical design and theory at the same university. Her doctoral supervisor is Prof. Kun Liu. Her research interests include surface and interface tribology and topography regulation.

Yunlong JIAO. He received his bachelor and Ph.D. degrees in mechanical engineering from Hefei University of Technology, Hefei, China, in 2012 and 2017, respectively. His doctoral supervisor is Prof. Kun Liu. He joined the Institute of Tribology at Hefei University of Technology from 2020. His current position is an associate professor. His research areas cover laser micro/nano fabrication and interface friction control.